Efficient Simultaneous Image Deconvolution and Upsampling Algorithm for Low Resolution Microwave Sounder Data

Jing Qin[a], **Igor Yanovsky**[b,c], **Wotao Yin**[a]

[a]**University of California, Los Angeles, Department of Mathematics, CA 90095, USA;**
[b]**Jet Propulsion Laboratory, California Institute of Technology, Pasadena, CA 91109, USA;**
[c] **Joint Institute for Regional Earth System Science and Engineering, University of California, Los Angeles, CA 90095, USA**

Abstract. Microwave imaging has been widely used in the prediction and tracking of hurricanes, typhoons, and tropical storms. Due to the limitations of the sensors, the acquired remote sensing data is usually blurry and has relatively low resolution, which calls for the development of fast algorithms for deblurring and enhancing the resolution. In this paper, we propose an efficient algorithm for simultaneous image deconvolution and upsampling for low resolution microwave hurricane data. The algorithm is derived by splitting the total variation regularization, the deconvolution operator and the upsampling operator in the objective in such a way that the alternating direction method of multipliers (ADMM) gives rise to three subproblems with closed-form solutions. We also extend the framework to the multichannel case with the multichannel total variation (mTV) regularization. A variety of numerical experiments on synthetic and real Advanced Microwave Sounding Unit (AMSU) and Microwave Humidity Sounder (MHS) data were conducted. The results demonstrate the outstanding performance of the proposed method.

Keywords: nonlinear image processing, deconvolution, resolution, microwaves, upsampling, Advanced Microwave Sounding Unit (AMSU), Microwave Humidity Sounder (MHS), alternating direction method of multipliers (ADMM).

Address all correspondence to: Jing Qin, University of California, Los Angeles, Department of Mathematics, 520 Portola Plaza, Los Angeles, CA 90095, USA; E-mail: jxq@ucla.edu

1 Introduction

Severe weather phenomena, such as hurricanes and tropical storms, can be continuously captured using geostationary microwave sensors. These sensors are designed to penetrate through thick clouds to record geophysical profiles of a storm, including temperature, humidity, water vapor, and cloud properties. The acquired images in a broad bandwidth are valuable for evaluating internal processes of the storm and its strength. For example, the Geostationary Synthetic Thinned Aperture Radiometer (GeoSTAR) is a microwave spectrometer aperture synthesis system that has been under development at Jet Propulsion Laboratory (JPL) since 1998 and will be used to capture hurricane imagery.[1] In principle, an aperture synthesis system is characterized by convolution with a point spread function (PSF), which is modeled as a two-dimensional sinc-like function. Due to the presence of positive and negative excursions in a PSF (cf. Fig. 1), there are ringing artifacts along sharp edges and other transitions in the observed field. It is of high necessity to process low-resolution physical weather systems. In the variational framework, we aim to solve the ill-posed *deconvolution and upsampling problem* to produce high-resolution images from blurry low-resolution data which may be polluted by the additive Gaussian noise.

In this paper, we use the data captured by the Microwave Humidity Sounder (MHS) instrument. MHS is a five-channel passive microwave radiometer, with frequencies ranging from 89 to 190 GHz, carried aboard meteorological satellites. It is similar in design to the Advanced Microwave Sounding Unit - B (AMSU-B) instrument, with some channel frequencies being slightly different from AMSU-B. The instrument examines several bands of microwave radiation and performs sounding of atmospheric physical properties. AMSU and MHS data have been used extensively in weather prediction, and long term AMSU and MHS records are used in climate studies.
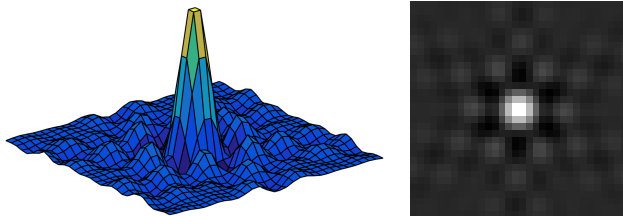

Fig 1 The GeoSTAR point spread function (PSF). A characteristic of an aperture synthesis system is that the PSF is a two-dimensional sinc-like function, showing positive and negative excursions, that produces ringing at sharp edges and other transitions in the observed field.

Motivated by the previous work,[2] this paper skillfully applies the alternating direction method of multipliers (ADMM) to solve the problem of image deconvolution and upsampling in a manner that all subproblems *have closed-form solutions*. In the single-channel case, we separate the three components in the objective functional–the total variation regularization, the deconvolution operator and the upsampling operator– and obtain three subproblems in the ADMM so that each has a closed-form solution. Among closely related work are[3] where upsampling is not being addressed, and[4] where different applications are considered. The multichannel case of our method considers the multichannel total variation (mTV) regularization and thereby has three subproblems in the ADMM that can be solved in closed forms. In particular, the solution to the subproblem involving mTV is given by the generalized shrinkage. Even though more computation is needed at each iteration, the proposed multichannel method takes fewer iterations to achieve convergence than the single-channel one.

The rest of the paper is organized as follows. Section 2 reviews the ADMM and total variation minimization. Section 3 describes the proposed splitting technique, applies the ADMM to derive the corresponding algorithm and discusses its convergence rates. Section 4 extends the proposed method to the multichannel deconvolution and upsampling model with the mTV regularization. Section 5 presents the numerical results on the synthetic AMSU and real MHS hurricane data. Finally, Section 6 concludes this paper and discusses future work.

2 Preliminaries

Since the ADMM was introduced by Glowinski and Marrocco[5] and Gabay and Mercier,[6] it has been widely applied to problems in imaging, statistical regression, machine learning, optimal control, and many other areas. To apply the ADMM, one must reformulate a problem into the form of

$$\min_{x,z} f(x) + g(z) \quad \text{s.t.} \quad Ax + Bz = c, \tag{1}$$

where x, z are unknown vectors, f, g are proper closed convex functions, A, B are matrices, and c is a given vector. (We restrict our discussion to Euclidean spaces.)

The ADMM is an *abstract algorithm* with two *subproblems*, one involving f and A and the other involving g and B, which must be solved at every iteration. There are many different approaches to reformulate a convex optimization problem into the form of (1), and they generally give rise to different subproblems (though they reduce to a few equivalence classes[7]).

Let us first review the ADMM. The augmented Lagrangian for the problem (1) is

$$L_\rho(x, z, y) := f(x) + g(z) + y^T(Ax + Bz - c) + \frac{\rho}{2} \|Ax + Bz - c\|_2^2,$$

where y is the dual variable. The ADMM seeks a solution to the problem (1) by iterating

$$\begin{cases} x^{k+1} \in \underset{x}{\operatorname{argmin}} \, L_\rho(x, z^k, y^k) & \text{(2a)} \\[2mm] z^{k+1} \in \underset{z}{\operatorname{argmin}} \, L_\rho(x^{k+1}, z, y^k) & \text{(2b)} \\[2mm] y^{k+1} = y^k + \gamma\rho(Ax^{k+1} + Bz^{k+1} - c), & \text{(2c)} \end{cases}$$

where $\rho > 0$ and the stepsize $\gamma \in (0, (\sqrt{5} + 1)/2)$ [8, Chapter 6]. Note that we could construct the following augmented Lagrangian

$$\widetilde{L}_\rho(x, z, y) := f(x) + g(z) + \frac{\rho}{2} \|Ax + Bz - c + y\|_2^2$$

which yields the same solution for the x-subproblem (2a) and the z-subproblem (2b) with the scaled update $y^{k+1} = y^k + \gamma(Ax^{k+1} + Bz^{k+1} - c)$. For the sake of simplification, we stick to the latter version in the entire paper. We use "$\in$" instead of "$=$" since the solutions x^{k+1} and z^{k+1} can be non-unique though different solutions will yield the same Ax^{k+1}, Bz^{k+1} and thus y^{k+1}. The ADMM has recently become a popular method for solving convex optimization problems arising in various application fields. It turned out to be equivalent to the Douglas-Rachford splitting iteration, a primal-dual iteration, and the ADMM itself applied to the Lagrange dual problem of (1) (see[7,9,10]).

Total variation minimization[11] is a well-known approach in regularized inverse problems and the recovery of images with sharp edges. In this paper, we use the isotropic version of the discrete total variation: $\text{TV}(u) = \|Du\|_1 = \sum_j \sqrt{(D_1 u)_j^2 + (D_2 u)_j^2}$ with the discrete finite difference operator $D = [D_1, D_2]$ satisfying the periodic boundary

conditions where $Du = [D_1u,\ D_2u]$. In addition to the traditional denoising problem,[11] the total variation minimization has been widely used in recovering images from their incomplete measurements.[12, 13] Typically, the corresponding optimization problem has the following form:

$$\min_{u} \|Du\|_1 + \frac{\mu}{2} \|Au - b\|_2^2, \tag{3}$$

where A is a sampling operator, b is the (noisy) observation of the true imaging under A, and $\mu > 0$ is a tuning parameter.

The use of variable splitting and the ADMM to total variation minimization and compressive sensing image recovery started in.[13, 14, 15] A dummy variable w is introduced to separate Du from $\|\cdot\|_1$, giving rise to the equivalent problem:

$$\min_{u,w} \|w\|_1 + \frac{\mu}{2} \|Au - b\|_2^2 \quad \text{s.t.} \quad w - Du = 0, \tag{4}$$

which is in the form of (1). It is recognized in[14] that when A and D are both convolution operators and satisfy the same boundary conditions, e.g., the periodic boundary conditions, a least-squares subproblem involving Au and Du has a closed-form solution via the diagonalization by the (discrete) Fourier transform. Such a least-squares subproblem arises in a quadratic penalty model in[14, 15] and the augmented Lagrangian method in.[13] It is worth noting that the ADMM has been skillfully applied to other image recovery problems in.[16, 17, 18, 19]

The problem of image deconvolution and upsampling studied in this paper has the form (3) with an operator A that composes sampling with convolution. Due to this composition, the least-squares subproblem that involves Au and Du no longer has a closed-form solution. We experimented solving the least-squares subproblem with the gradient descent method in[3] and recognized a strong need for better performance. In this paper, we introduce a much more efficient method by reformulating the problem and obtaining an ADMM algorithm with three subproblems, all of which have closed-form solutions.

3 Proposed Image Deconvolution and Upsampling Algorithm

Without loss of generality and for presentation simplicity, we assume a square image domain. Let $u_0 \in \mathbb{R}^{n^2}$ be the ground truth image to be reconstructed, and $K : \mathbb{R}^{n^2} \to \mathbb{R}^{n^2}$ be a discrete convolution operator associated with the point spread function k. The observed blurry and noisy low-resolution image $b \in \mathbb{R}^m$ $(m < n^2)$ satisfies

$$b = K_p u_0 + \text{noise},$$

where K_p is the composition of the convolution and the sampling operators, i.e., $K_p = PK$. The two-dimensional convolution operator K corresponds to the block circulant matrix in the following sense

$$\text{vec}(k * v) = K\text{vec}(v), \quad v \in \mathbb{R}^{n \times n}.$$

To reconstruct u_0, we consider the following total variation based minimization problem

$$\min_{u} \|Du\|_1 + \frac{\mu}{2} \|PKu - b\|_2^2, \tag{5}$$

where $D : \mathbb{R}^{n^2} \to \mathbb{R}^{2n^2}$ is the finite difference operator following the periodic boundary conditions and μ is a parameter related to the noise level. The solution u of (5) is an estimate of u_0.

Unlike the conventional deconvolution models, the non-circulant structure of P will make it difficult to solve the least-squares u-subproblem if we directly apply the ADMM. By introducing $w = Ku$, we split P and K (in the sense that they are applied to different variables) as follows:

$$\min_{u,v,w} \|v\|_1 + \frac{\mu}{2} \|Pw - b\|_2^2 \quad \text{s.t.} \quad Du - v = 0, \quad w - Ku = 0. \tag{6}$$

Then the augmented Lagrangian is

$$L_{\rho_1,\rho_2}(u, v, w, x, y) = \|v\|_1 + \frac{\mu}{2} \|Pw - b\|_2^2 + \frac{\rho_1}{2} \left(\|Du - v + x\|_2^2 + \frac{\rho_2}{\rho_1} \|w - Ku + y\|_2^2 \right),$$

where x and y are the *scaled* dual variables, scaled by ρ_1, ρ_2, respectively, so they appear in the quadratic penalty terms. The scaled alternating direction method of multipliers (ADMM) yields the following iteration

$$
\begin{cases}
(v^{k+1}, w^{k+1}) = \underset{v,w}{\operatorname{argmin}}\, L_{\rho_1,\rho_2}(u^k, v, w, x^k, y^k) & \text{(7a)} \\[2mm]
u^{k+1} = \underset{u}{\operatorname{argmin}}\, L_{\rho_1,\rho_2}(u, v^{k+1}, w^{k+1}, x^k, y^k) & \text{(7b)} \\[2mm]
x^{k+1} = x^k + \gamma(Du^{k+1} - v^{k+1}) & \text{(7c)} \\[2mm]
y^{k+1} = y^k + \gamma(w^{k+1} - Ku^{k+1}). & \text{(7d)}
\end{cases}
$$

Due to the separability of variables v and w in the first subproblem, we are able to update v and w individually.

- **v-subproblem:**

$$
v^{k+1} = \underset{v}{\operatorname{argmin}}\, \|v\|_1 + \frac{\rho_1}{2}\left\| Du^k - v + x^k \right\|_2^2
$$

can be solved in the closed form as

$$
v^{k+1} = \operatorname{shrink}(Du^k + x^k, 1/\rho_1),
$$

where $\operatorname{shrink}(v, \sigma) = \operatorname{sgn}(v) \odot \max(|v| - \sigma, 0)$ with componentwise multiplication $\odot$.

- **w-subproblem:**

$$
w^{k+1} = \underset{w}{\operatorname{argmin}}\, \frac{\mu}{2}\|Pw - b\|_2^2 + \frac{\rho_2}{2}\left\| w - Ku^k + y^k \right\|_2^2
$$

reduces to the normal equations:

$$
\mu P^T(Pw - b) + \rho_2(w - Ku^k + y^k) = 0,
$$

which again can be solved in the closed form as

$$
w = (\mu P^T P + \rho_2 I)^{-1}(\mu P^T b + \rho_2(Ku^k - y^k)),
$$

or equivalently

$$
\begin{cases}
w \leftarrow Ku^k - y^k \\
w_P \leftarrow (\mu b + \rho_2 w_P)/(\mu + \rho_2).
\end{cases}
\tag{8}
$$

Here w_P represents the subvector of w with the index set specified by the sampling operator P. In the noise-free case where the w-subproblem has an equality constraint

$$
w = \underset{w}{\operatorname{argmin}}\, \frac{\rho_2}{2}\left\| w - Ku^k + y^k \right\|_2^2 \quad \text{s.t.} \quad Pw = b,
$$

the solution can be obtained by

$$
\begin{cases}
w \leftarrow Ku^k - y^k \\
w_P \leftarrow b.
\end{cases}
\tag{9}
$$

In fact, this is the projection of the least-square solution $Ku^k - y^k$ to the hyperspace $\{w : Pw = b\}$.

- **u-subproblem:**

$$
u^{k+1} = \underset{u}{\operatorname{argmin}}\, \frac{\rho_1}{2}\left\| Du - v^{k+1} + x^k \right\|_2^2 + \frac{\rho_2}{2}\left\| w^{k+1} - Ku + y^k \right\|_2^2
$$

reduces to the normal equations

$$
\rho_1 \sum_{i=1}^{2} D_i^T(D_i u - v_i^{k+1} + x_i^k) + \rho_2 K^T(Ku - w^{k+1} - y^k) = 0,
$$

which can be solved in the closed form by applying the two-dimensional discrete Fourier transform as follows:

$$u = F^* \left(\frac{\rho_1 \sum_{i=1}^{2} F D_i^T (v_i^{k+1} - x_i^k) + \rho_2 F K^T (w^{k+1} + y^k)}{\rho_1 \sum_{i=1}^{2} \mathrm{diag}(F D_i^T D_i F^*) + \rho_2 \mathrm{diag}(F K^T K F^*)} \right), \tag{10}$$

where the operator $\mathrm{diag} : \mathbb{R}^{n^2} \times \mathbb{R}^{n^2} \to \mathbb{R}^{n^2}$ extracts all diagonal entries of a square matrix as a vector, the matrix $F \in \mathbb{C}^{n^2 \times n^2}$ is generated by Kronecker product of the one-dimensional discrete Fourier transformation matrix $F_n \in \mathbb{C}^{n \times n}$ and itself, and the division is applied componentwise. Note that although matrix-vector multiplication is involved in (10), we apply the two-dimensional fast Fourier transform (FFT) directly to the image in the numerical implementation. Since K represents the convolution operator under the periodic boundary conditions, i.e., $Ku = k \otimes u$, the matrix $FK^T K F^*$ can be efficiently computed by FFT. Under general boundary conditions for the convolution operator, especially non-circulant K, we could decompose $K = K_1 + K_2$ where K_1 is still circulant and K_2 is sparse added to correct the boundary conditions.[20]

The convergence of the ADMM has been long proved in [8, Chapter 6]. We apply the results from the papers[21, 22] to obtain the following rates:

- The violation to the constraints in the problem (6) $\|Du^k - v^k\|^2 + \|w^k - Ku^k\|^2$ reduces at the rate of $o(1/k)$, and if we replace u^k by the running average $\bar{u}^k = \frac{1}{k} \sum_{i=1}^{k} u^i$ and replace v^k and w^k by their running averages as well, then the rate improves to $O(1/k^2)$. The latter is known as the ergodic rate. Note that the violation is not monotonic in general.

- Let $\eta_k := \|v^k\|_1 + \frac{\mu}{2} \|Pw^k - b\|_2$ and $\eta^* := \|Du^*\|_1 + \frac{\mu}{2} \|PKu^* - b\|_2$. Then, the objective error $|\eta_k - \eta^*|$ reduces at the rate of $o(1/\sqrt{k})$, and the corresponding ergodic rate improves to $O(1/k)$. Note that it is possible that $\eta_k < \eta^*$ due to constraint violation.

4 Multichannel Extension

When the underlying data has multiple channels, we extend the deconvolution and upsampling model (5) by choosing the mTV as the regularization term. Instead of processing the data channel by channel, the mTV couples various channels and ensures consistent regularity across the channels. More specifically, let $\mathbf{u} = (u_1, \ldots, u_c)^T$ with each $u_i \in \mathbb{R}^{n^2}$, and generalize the model (5) to the following form:

$$\min_{\mathbf{u}} \|\mathbf{u}\|_{mTV} + \frac{\mu}{2} \sum_{i=1}^{c} \|PKu_i - b_i\|_2^2. \tag{11}$$

Here the mTV semi-norm of $\mathbf{u}$ is defined as

$$\|\mathbf{u}\|_{mTV} = \sum_j \sqrt{\sum_{i=1}^{c} |(Du_i)_j|^2}.$$

Let D_1 and D_2 be the difference operators along the x-axis and the y-axis, respectively. Here we use the isotropic total variation at each pixel defined in Section 2. Similar to (6), we split the regularization term and the fidelity term as follows

$$\min_{\mathbf{u}, \mathbf{v}, \mathbf{w}} \|\mathbf{v}\|_{mTV} + \frac{\mu}{2} \sum_{i=1}^{c} \|Pw_i - b_i\|_2^2 \quad \text{s.t.} \quad Du_i - v_i = 0, \quad w_i - Ku_i = 0, \quad i = 1, \ldots, c. \tag{12}$$

With the augmented Lagrangian defined by

$$L_{\rho_1, \rho_2}(\mathbf{u}, \mathbf{v}, \mathbf{w}, \mathbf{x}, \mathbf{y}) = \|\mathbf{v}\|_{mTV} + \frac{\mu}{2} \sum_{i=1}^{c} \|Pw_i - b_i\|_2^2 + \sum_{i=1}^{c} \left(\frac{\rho_1}{2} \|Du_i - v_i + x_i\|_2^2 + \frac{\rho_2}{2} \|w_i - Ku_i + y_i\|_2^2 \right),$$

we obtain the following ADMM iteration:

$$\begin{cases} (\mathbf{v}^{k+1}, \mathbf{w}^{k+1}) = \underset{\mathbf{v},\mathbf{w}}{\operatorname{argmin}} \, L_{\rho_1,\rho_2}(\mathbf{u}^k, \mathbf{v}, \mathbf{w}, \mathbf{x}^k, \mathbf{y}^k) & \text{(13a)} \\[2mm] \mathbf{u}^{k+1} = \underset{\mathbf{u}}{\operatorname{argmin}} \, L_{\rho_1,\rho_2}(\mathbf{u}, \mathbf{v}^{k+1}, \mathbf{w}^{k+1}, \mathbf{x}^k, \mathbf{y}^k) & \text{(13b)} \\[2mm] x_i^{k+1} = x_i^k + \gamma(Du_i^{k+1} - v_i^{k+1}), \quad i = 1, \ldots, c. & \text{(13c)} \\[2mm] y_i^{k+1} = y_i^k + \gamma(w_i^{k+1} - Ku_i^{k+1}), \quad i = 1, \ldots, c. & \text{(13d)} \end{cases}$$

Similar to the analysis in Section 3, each subproblem has a closed-form solution. In particular, the $\mathbf{v}$-subproblem has the solution represented by the generalized shrinkage operator

$$v_i^{k+1} = \frac{Du_i^k + x_i^k}{s_k} \max\left\{s_k - \frac{1}{\rho_1}, \mathbf{0}\right\}, \quad i = 1, \ldots, c,$$

where

$$s_k = \sqrt{\sum_{i=1}^{c} \left\| Du_i^k + x_i^k \right\|_2^2}.$$

Each component w_i is updated via (8) or (9) depending on the noise level. Similar to the derivation of (10), by letting $x_i = (x_{i,1}, x_{i,2})^T$ and $v_i = (v_{i,1}, v_{i,2})^T$ with $x_{i,j}, v_{i,j} \in \mathbb{R}^{n^2}$ for $i = 1, \ldots, c$ and $j = 1, 2$, we obtain the following solution to the $\mathbf{u}$-subproblem:

$$u_i = F^*\left(\frac{\rho_1 \sum_{j=1}^{2} FD_j^T(v_{i,j}^{k+1} - x_{i,j}^k) + \rho_2 FK^T(w_i^{k+1} + y_i^k)}{\rho_1 \sum_{j=1}^{2} \operatorname{diag}(FD_j^T D_j F^*) + \rho_2 \operatorname{diag}(FK^T KF^*)} \right), \quad i = 1, \ldots, c. \tag{14}$$

5 Numerical Results

This section presents the numerical results obtained by applying the proposed algorithms on various synthetic and real data of severe weather phenomena. The 32×32 discretized GeoSTAR point spread function depicted on Fig. 1 was chosen as the blurring kernel for all tests. To measure performance, we use the relative error defined by

$$Relerr = \frac{\|u - \hat{u}\|_2}{\|u\|_2}$$

where $u \in \mathbb{R}^{n^2}$ is the ground truth image and $\hat{u}$ is the recovered image. All experiments were run in Matlab 2013a on a desktop computer with 8GB of RAM and a 3.10GHz Intel i7-4770S CPU. All parameters are chosen to yield the best performance.

In the first experiment, we used simulated microwave images of the 2005 Atlantic hurricane Rita shown on Fig. 2 and 3. By default, all images are displayed in the range $[110, 285]$ in Kelvin. Fig. 2 shows 50.3, 52.8, 53.6, 54.4, 54.9, 55.5 GHz, and Fig. 3 shows 150, 157, 166, 176, 180, 182 GHz channel images. For comparison, GeoSTAR operates at some of the same frequencies of the Advanced Microwave Sounding Unit - A (AMSU-A) and - B (AMSU-B) temperature and humidity sounders near 55 GHz and 180 GHz, respectively. The images have 400×400 pixels and were derived from cloud resolving numerical weather prediction model (WRF)[23,24] simulations. A standard radiative transfer model was used to generate the brightness temperatures from the WRF fields. The resolution of a pixel is 1.3 km. With this grid spacing, we are able to resolve features that are approximately 5 km wide.

Fig. 4 and Fig. 5 depict images of Fig. 2 and 3 blurred with GeoSTAR kernel as well as the results after applying the proposed algorithm to the blurry low-resolution data. We choose the downsampling factor $r = 2$ and 3, i.e., downsampling the 402×402 blurry images into the 201×201 and 134×134 ones, respectively. Note that the selected downsampling factors, i.e 2 and 3, are most commonly used in applications, as larger downsampling factors produce results that are not so accurate. The corresponding comparison of relative errors are shown in Table 1. From the results, one can see that as the image has more fine features, the reconstruction becomes more difficult as reflected in the increase of relative error. On the contrary, if the image to be recovered is more piecewise constant, the reconstruction has smaller relative error. In Table 2, we show the results by fixing the sampling factor as two and varying the noise level as $\sigma = 5, 10, 15$.
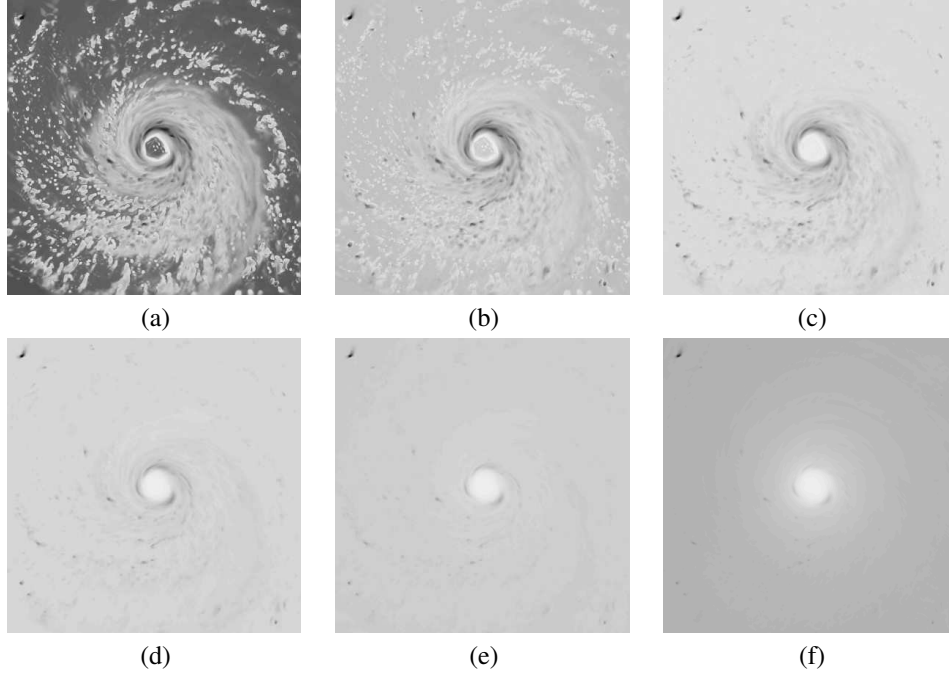
Fig 2 Original microwave channels of the simulated hurricane Rita image. (a) to (f) correspond to 50.3, 52.8, 53.6, 54.4, 54.9, 55.5 GHz.
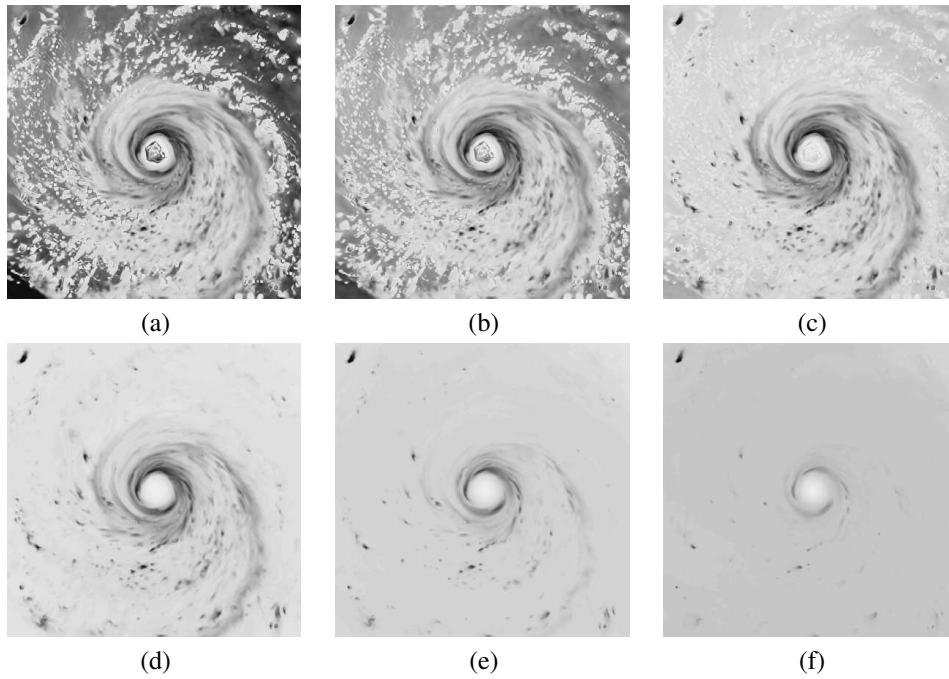

Fig 3 Original microwave channels of the simulated hurricane Rita image. (a) to (f) correspond to 150, 157, 166, 176, 180, 182 GHz.

Channel (GHz)	$r = 2$	$r = 3$	Channel (GHz)	$r = 2$	$r = 3$
50.3	0.0392	0.0713	150	0.0515	0.0837
52.8	0.0098	0.0167	157	0.0339	0.0538
53.6	0.0038	0.0072	166	0.0140	0.0222
54.4	0.0021	0.0040	176	0.0071	0.0126
54.9	0.0015	0.0026	180	0.0040	0.0074
55.5	0.0014	0.0024	182	0.0024	0.0039

Table 1 Relative error comparison for the simulated hurricane Rita data with sampling factors $r = 2$ and 3.

Channel (GHz)	$\sigma = 5$	$\sigma = 10$	$\sigma = 15$	Channel (GHz)	$\sigma = 5$	$\sigma = 10$	$\sigma = 15$
50.3	0.0816	0.0926	0.1013	150	0.0882	0.0988	0.1049
52.8	0.0292	0.0325	0.0440	157	0.0594	0.0666	0.0741
53.6	0.0234	0.0258	0.0374	166	0.0321	0.0363	0.0464
54.4	0.0234	0.0250	0.0371	176	0.0262	0.0294	0.0403
54.9	0.0229	0.0257	0.0383	180	0.0247	0.0272	0.0391
55.5	0.0265	0.0289	0.0432	182	0.0251	0.0273	0.0404

Table 2 Relative error comparison for the simulated hurricane Rita data with various noise levels and fixed sampling factor $r = 2$. For all tests, $\mu = 10^{-8}$, $\rho_1 = 10^{-6}$. Here ρ_2 is set to 10^{-6} when $\sigma = 5$ and 10^{-7} otherwise.

In Fig. 6 and Fig. 7, we tested the proposed method on real MHS data of the 2005 Atlantic hurricane Katrina and the 2005 Pacific typhoon Talim, respectively. Each image has five frequency bands at 89, 150, 183±1, 183±3, and 183±7 GHz. The resolution of each pixel is 15 km. We used sampling factor $r = 2, 3$ in our experiments. The corresponding relative errors are shown in Table 3.

Channel (GHz)	Katrina		Talim	
	$r = 2$	$r = 3$	$r = 2$	$r = 3$
89	0.0242	0.0392	0.0252	0.0396
157	0.0349	0.0567	0.0186	0.0304
183±1	0.0208	0.0297	0.0170	0.0230
183±3	0.0248	0.0401	0.0155	0.0240
190	0.0293	0.0490	0.0167	0.0273

Table 3 Relative error comparison of hurricane Katrina and typhoon Talim MHS channels with sampling factors $r = 2$ and 3. Note that for $r = 2$, $\rho_2 = 10^{-3}$, and all other parameters are set the same as those specified in Fig. 6 and Fig. 7 when $r = 3$.

Finally, we tested the proposed multichannel algorithm (12) on three sets of data with sampling factors $r = 2, 3$. The performance comparison in terms of relative error for each channel are listed in Tables 4 and 5. Comparing these results with those obtained by the single channel algorithm in Tables 1 and 3, one can see that the mTV is able to enhance the reconstruction quality for those channels with more fine features while trading the quality of the channels with less features. In addition, Table 6 compares the average running time in seconds per iteration for each data set using the proposed single-channel algorithm and the multichannel algorithm. Note that the multichannel algorithm usually uses far less iterations (200∼400) to reach a desired result while its single-channel counterpart uses various numbers of iterations (200∼1000) for each channel and some channels need a lot more iterations to achieve the desired accuracy. Nevertheless, both versions are very efficient so that the reconstruction of an image is achieved at the rate of about 2.5×10^{-7} per pixel per iteration.

Channel (GHz)	$r = 2$	$r = 3$	Channel (GHz)	$r = 2$	$r = 3$
50.3	0.0377	0.0696	150	0.0496	0.0828
52.8	0.0095	0.0165	157	0.0320	0.0532
53.6	0.0044	0.0077	166	0.0136	0.0229
54.4	0.0024	0.0042	176	0.0076	0.0138
54.9	0.0017	0.0028	180	0.0046	0.0086
55.5	0.0018	0.0025	182	0.0029	0.0048

Table 4 Relative error comparison for the simulated hurricane Rita data using the multichannel Algorithm (12). When $r = 2$, $\mu = 10^{-3}$ and $\rho_1 = 10$, and $\rho_2 = 10^{-1}$. When $r = 3$, $\mu = 10^{-4}$, $\rho_1 = 10$ and $\rho_2 = 10^{-3}$.

Channel (GHz)	Katrina		Talim	
	$r = 2$	$r = 3$	$r = 2$	$r = 3$
89	0.0244	0.0391	0.0241	0.0385
157	0.0347	0.0569	0.0189	0.0307
183±1	0.0200	0.0289	0.0167	0.0223
183±3	0.0238	0.0393	0.0151	0.0235
190±7	0.0283	0.0485	0.0163	0.0271

Table 5 Relative error comparison of hurricane Katrina and typhoon Talim MHS data using the multichannel Algorithm (12). For all tests, $\mu = 10^{-4}$ and $\rho_1 = 10$. We choose $\rho_2 = 10^{-2}$ when $r = 2$ and 10^{-3} when $r = 3$.

	Rita 402×402	Katrina 150×90	Talim 210×90
Single-channel	0.0450	0.0038	0.0044
Multichannel	0.3383	0.0187	0.0239

Table 6 Comparison of running time in seconds per iteration.

6 Conclusions

We proposed an efficient deconvolution and upsampling method for the hurricane microwave data, and extended it to handle multichannel data by using the mTV regularization. Derived from proper variable splitting and the ADMM, the proposed algorithms provide simple subproblems and fast convergence, and produce high resolution images with small reconstruction errors. The experiments on the synthetic microwave data demonstrate the great potential of our work. Our technique can be easily adapted or extended to address other ill-posed problems for applications dealing with large-scale data sets. For the future work, the weighted mTV with adaptive weights can be considered to improve the smoothness for each channel. Taking the texture-like features in the microwave hurricane images into account, the multi-resolution transformation based regularization will be worth exploring as well.

References

1 Alan B Tanner, William J Wilson, Bjorn H Lambrigsten, Steve J Dinardo, Shannon T Brown, Pekka P Kangaslahti, Todd C Gaier, Christopher S Ruf, Steven M Gross, Boon H Lim, et al. Initial results of the Geostationary Synthetic Thinned Array Radiometer (GeoSTAR) demonstrator instrument. *Geoscience and Remote Sensing, IEEE Transactions on*, 45(7):1947–1957, 2007.

2 Wotao Yin, Simon Morgan, Junfeng Yang, and Yin Zhang. Practical compressive sensing with Toeplitz and circulant matrices. In *Visual Communications and Image Processing 2010*, pages 77440K–77440K. International Society for Optics and Photonics, 2010.

3 Igor Yanovsky, Alan Tanner, and Bjorn Lambrigtsen. Efficient deconvolution and spatial resolution enhancement from continuous and oversampled observations in microwave imagery. In *Microwave Radiometry and Remote Sensing of the Environment (MicroRad), 2014 13th Specialist Meeting on*, pages 151–156. IEEE, 2014.

4 Zhida Shen, Zhe Geng, and Junfeng Yang. Image reconstruction from incomplete convolution data via total variation regularization. *Statistics, Optimization & Information Computing*, 3(1):1–14, 2015.

5 R. Glowinski and A. Marrocco. Sur l'approximation, par elements finis d'ordre un, et la resolution, par, penalisation-dualité, d'une classe de problems de dirichlet non lineares. *Revue Française d'Automatique, Informatique, et Recherche Opéationelle*, 9:41–76, 1975.

6 D. Gabay and B. Mercier. A dual algorithm for the solution of nonlinear variational problems via finite element approximations. *Computers and Mathematics with Applications*, 2(1):17–40, 1976.

7 Ming Yan and Wotao Yin. Self Equivalence of the Alternating Direction Method of Multipliers. *arXiv preprint arXiv:1407.7400*, 2014.

8 Roland Glowinski and JT Oden. Numerical methods for nonlinear variational problems. *Journal of Applied Mechanics*, 52:739, 1985.

9 Daniel Gabay. Chapter ix applications of the method of multipliers to variational inequalities. *Studies in mathematics and its applications*, 15:299–331, 1983.

10 Antonin Chambolle and Thomas Pock. A first-order primal-dual algorithm for convex problems with applications to imaging. *Journal of Mathematical Imaging and Vision*, 40(1):120–145, 2011.

11 Leonid I Rudin, Stanley Osher, and Emad Fatemi. Nonlinear total variation based noise removal algorithms. *Physica D: Nonlinear Phenomena*, 60(1):259–268, 1992.

12 Emmanuel J Candes, Justin K Romberg, and Terence Tao. Stable signal recovery from incomplete and inaccurate measurements. *Communications on pure and applied mathematics*, 59(8):1207–1223, 2006.

13 Tom Goldstein and Stanley Osher. The split Bregman method for L1-regularized problems. *SIAM Journal on Imaging Sciences*, 2(2):323–343, 2009.

14 Yilun Wang, Junfeng Yang, Wotao Yin, and Yin Zhang. A new alternating minimization algorithm for total variation image reconstruction. *SIAM Journal on Imaging Sciences*, 1(3):248–272, 2008.

15 Junfeng Yang, Yin Zhang, and Wotao Yin. A fast alternating direction method for TVL1-L2 signal reconstruction from partial Fourier data. *Selected Topics in Signal Processing, IEEE Journal of*, 4(2):288–297, 2010.

16 Xiaojing Ye, Yunmei Chen, and Feng Huang. Computational acceleration for MR image reconstruction in partially parallel imaging. *Medical Imaging, IEEE Transactions on*, 30(5):1055–1063, 2011.

17 Junfeng Yang and Yin Zhang. Alternating direction algorithms for ℓ_1-problems in compressive sensing. *SIAM journal on scientific computing*, 33(1):250–278, 2011.

18 Yunmei Chen, William Hager, Feng Huang, Dzung Phan, Xiaojing Ye, and Wotao Yin. Fast algorithms for image reconstruction with application to partially parallel MR imaging. *SIAM Journal on Imaging Sciences*, 5(1):90–118, 2012.

19 Yunmei Chen, William W Hager, Maryam Yashtini, Xiaojing Ye, and Hongchao Zhang. Bregman operator splitting with variable stepsize for total variation image reconstruction. *Computational Optimization and Applications*, 54(2):317–342, 2013.

20 Daniel O'Connor and Lieven Vandenberghe. Primal-Dual Decomposition by Operator Splitting and Applications to Image Deblurring. *SIAM Journal on Imaging Sciences*, 7(3):1724–1754, 2014.

21 Damek Davis and Wotao Yin. Convergence rate analysis of several splitting schemes. *arXiv preprint arXiv:1406.4834*, 2014.

22 Damek Davis and Wotao Yin. Convergence rates of relaxed Peaceman-Rachford and ADMM under regularity assumptions. *arXiv preprint arXiv:1407.5210*, 2014.

23 J. Michalakes, J. Dudhia, D.O. Gill, J.B. Klemp, and W. Skamarock. Design of a next-generation regional weather research and forecast model. *Towards teracomputing*, pages 117–124, 1998.

24 J. Michalakes, J. Dudhia, D.O. Gill, T.B. Henderson, J.B. Klemp, W. Skamarock, and W. Wang. The weather research and forecast model: Software architecture and performance. In *11th ECMWF Workshop on the Use of High Performance Computing in Meteorology*, Reading, United Kingdom, October 2004.
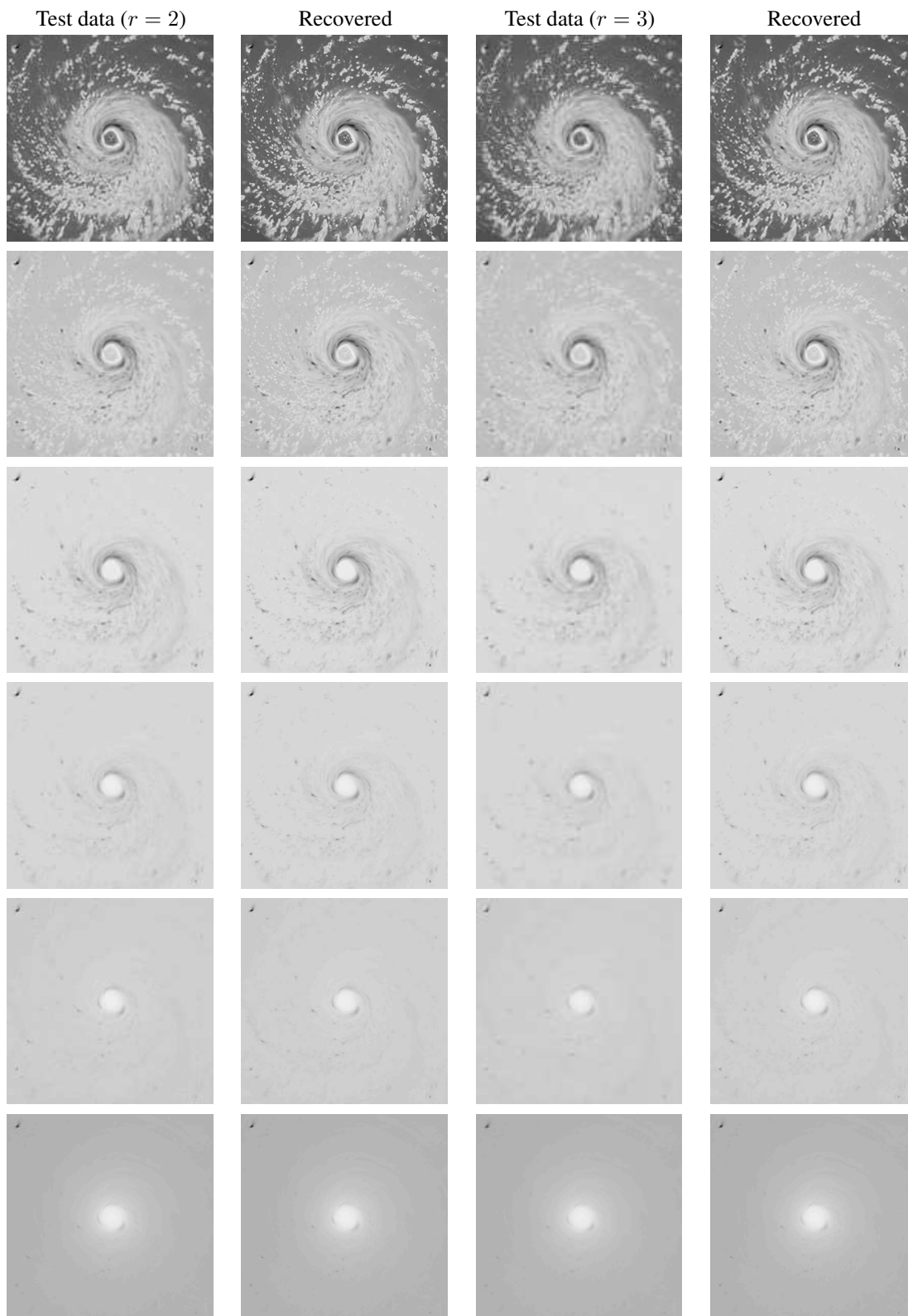
Fig 4 Tests on the simulated hurricane Rita data with sampling factors $r = 2$ and 3. From top to bottom: 50.3, 52.8, 53.6, 54.4, 54.9, 55.5 GHz channels. If $r = 2$, then $\mu = 10^{-3}$, $\rho_1 = 10$ and $\rho_2 = 10^{-2}$. If $r = 3$, then $\mu = 10^{-4}$, $\rho_1 = 10$ and $\rho_2 = 10^{-4}$.
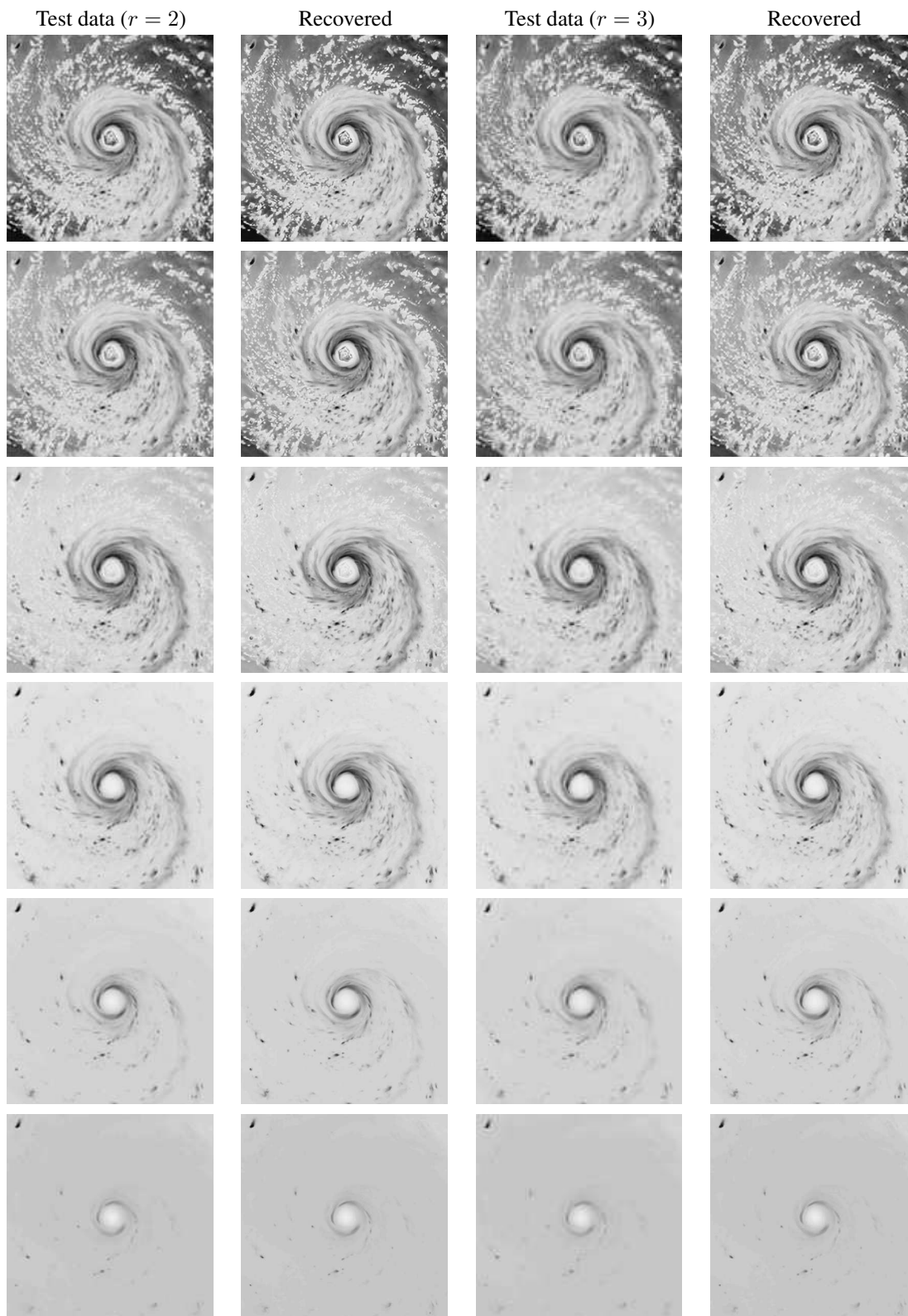
Test data ($r = 2$)	Recovered	Test data ($r = 3$)	Recovered

Fig 5 Tests on the simulated hurricane Rita data with sampling factors $r = 2$ and 3. From top to bottom: 150, 157, 166, 176, 180, 182 GHz channels. Here we choose $\mu = 10^{-4}$, $\rho_1 = 10$ and $\rho_2 = 10^{-4}$.
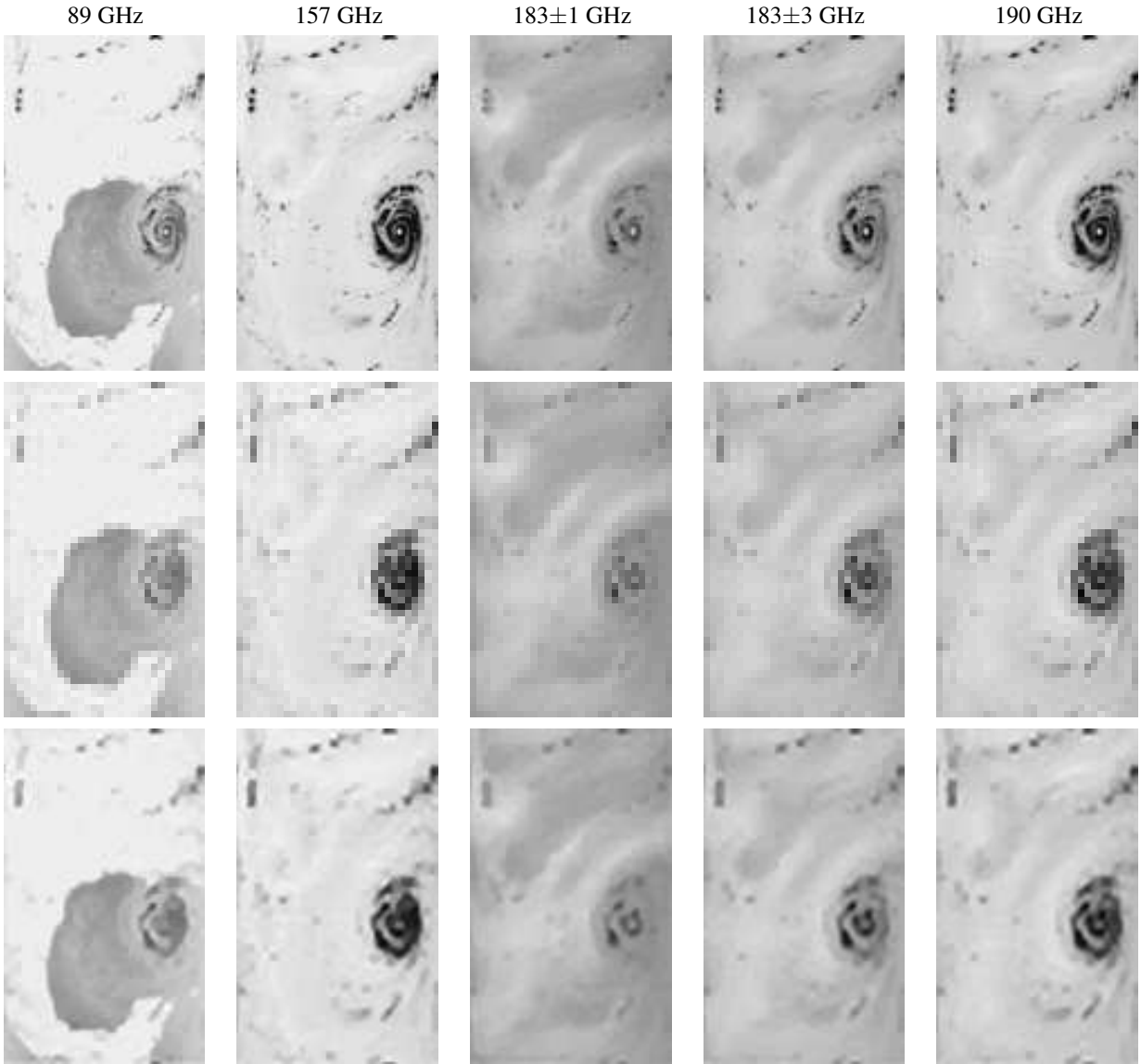
Fig 6 Tests on hurricane Katrina MHS 89, 157, 183±1, 183±3, 190 GHz channels with sampling factor $r = 3$. From top to bottom: ground truth images, blurry data with downsampling factor $r = 3$, and the recovered images. Here we choose $\mu = 10^{-4}$, $\rho_1 = 10$ and $\rho_2 = 10^{-4}$.
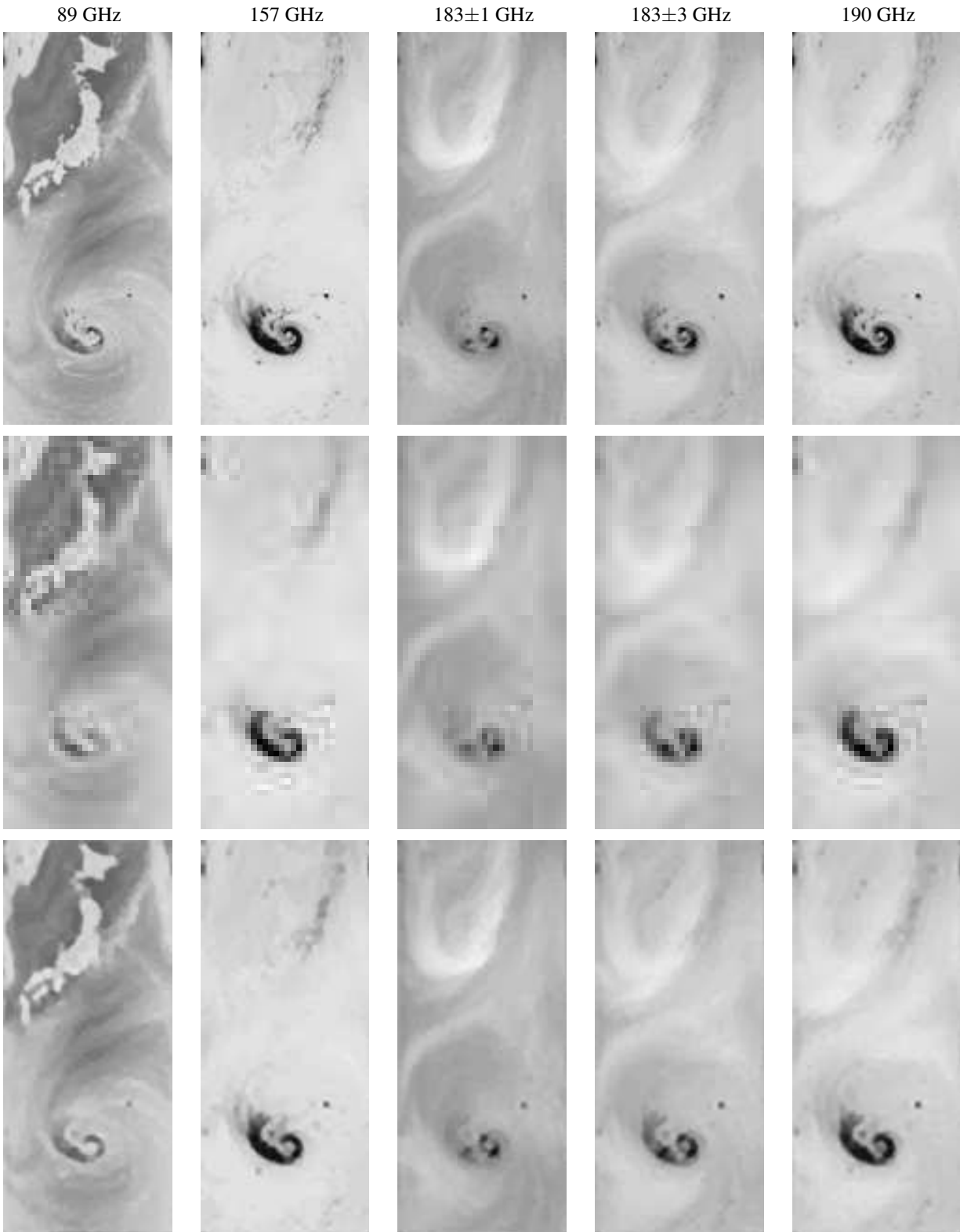
Fig 7 Tests on typhoon Talim MHS 89, 157, 183±1, 183±3, 190 GHz channels with sampling factor $r = 3$. From top to bottom: ground truth images, blurry data with downsampling factor $r = 3$, and the recovered images. Here we choose $\mu = 10^{-4}$, $\rho_1 = 10$ and $\rho_2 = 10^{-4}$.